International Journal of Nanoelectronics and Materials
IJNeaM
ISSN 198-5761 | E-ISSN 2232-1535

# Catalytic Effect of Iron (III) Nitrate on the Synthesis of Reduced Graphene Oxide from Oil Palm Kernel Shell-Derived Graphite

Ismariza Ismail[a,b,*], N. A. Karim[a,c], Adilah Ayoib[a,b], Oo Cheng Hong[b], Muhammad M. Ramli[a,d], Shazlina Johari[a,d], Anis Syafiqa Rosman[d], Nurul Aishah Mohd Amran[d]

[a]*Institute of Nano Electronic Engineering, Universiti Malaysia Perlis, 01000 Kangar, Malaysia*
[b]*Faculty of Chemical Engineering & Technology, Universiti Malaysia Perlis, 02600 Arau, Malaysia*
[c]*Faculty of Mechanical Engineering & Technology, Universiti Malaysia Perlis, 02600 Arau, Malaysia*
[d]*Faculty of Electrical Engineering & Technology, Universiti Malaysia Perlis, 02600 Arau, Malaysia*
**Corresponding author. Tel.: +6-012-647-5992; e-mail: ismariza@unimap.edu*

Received 18 Jul 2025, Revised 5 May 2025, Accepted 21 May 2026

**ABSTRACT**

This study investigates the catalytic role of iron (III) nitrate [$Fe(NO_3)_3$] in synthesizing reduced graphene oxide (rGO) from graphite derived from oil palm kernel shell (OPKS) biomass. OPKS was impregnated with $Fe(NO_3)_3$ at concentrations of 0, 10, 20, and 30 wt.% (samples $G_0$, $G_{10}$, $G_{20}$, and $G_{30}$), and were subsequently pyrolyzed for catalytic graphitization. X-ray diffraction (XRD) results showed $G_{20}$, which was prepared with 20 wt.% catalyst, achieved the highest degree of graphitization (97%) and a near-ideal interlayer spacing of 0.344 nm, as indicated by sharp, intense diffraction peaks. Graphite samples, $G_0$ and $G_{20}$, were oxidized via a modified Hummers' method to obtain GO, then chemically reduced to yield $rGO_0$ and $rGO_{20}$. Raman spectroscopy, SEM, and XRD characterization confirmed that $rGO_{20}$ exhibited superior graphitic features compared to $rGO_0$, which includes a lower defect density reflected by a reduced $I_D/I_G$ ratio from 1.155 to 1.128, sharper XRD reflections, and larger, well- defined pores. Collectively, these results highlight the critical influence of $Fe(NO_3)_3$ concentration in enhancing precursor graphite crystallinity and, consequently, the structural quality of the derived rGO. Catalytic graphitization at 20 wt.% $Fe(NO_3)_3$ thus provides an effective and sustainable route for producing high-quality rGO from renewable biomass resources, with promising implications for energy storage and advanced functional material applications.

**Keywords:** *Biomass-derived graphite, reduced graphene oxide, rGO, catalytic graphitization, oil palm kernel shell*

## 1. INTRODUCTION

Reduced graphene oxide (rGO) is a two-dimensional nanomaterial derived from graphite oxide and belongs to the family of carbon allotropes. Carbon can exist in different structural arrangements, including diamond, graphite, graphene, amorphous carbon, and carbon nanotubes. Among them, graphene and its derivatives, graphene oxide (GO) and rGO, have gained considerable attention due to their unique properties. rGO does not occur naturally but is produced by manipulating carbon structures at the atomic level [1].

Structurally, rGO consists of carbon atoms arranged in a two-dimensional honeycomb lattice, conferring remarkable mechanical strength, high electrical conductivity, and chemical stability. Compared to GO, rGO contains fewer oxygen functional groups (such as hydroxyl, carbonyl, ester, and acyl groups), resulting in improved graphitic ordering, higher electrical conductivity, and greater thermal stability [2], [3], [4]. These features also enhance its mechanical robustness, making rGO more suitable than GO for practical applications. Consequently, rGO is widely studied for supercapacitors, lithium-ion batteries, sensors, optoelectronics, and environmental remediation, as well as biomedical applications due to its biocompatibility and antibacterial properties [5], [6].

rGO is typically produced from graphite through oxidation to GO, followed by reduction. Graphite oxidation introduces oxygen-containing groups that disrupt the lattice, enabling exfoliation into GO sheets, which can then be reduced to rGO. Several synthesis routes exist, including mechanical exfoliation, chemical vapor deposition (CVD), and chemical oxidation via the modified Hummers' method [7], [8], [9]. Among the synthesis routes, the modified Hummers' method is most widely used due to its relatively high yield and practicality.

While natural graphite is typically mined, synthetic graphite can be obtained from petroleum-based feedstocks or renewable biomass [10]. Biomass is particularly attractive as a sustainable, cost-effective, and renewable precursor [11]. Various types of biomasses have been successfully investigated for graphite and graphene production, including rice husks, sugarcane bagasse, sawdust, bamboo, coconut shells, and agricultural residues such as corncobs and wheat straw. These materials are rich in carbon and, when pyrolysed, can yield graphitic structures suitable for further processing. Biomass sources that are especially high in cellulose and hemicellulose, such as bamboo, pine sawdust, and lignin-rich plant matter, are particularly favorable for graphitization due to their ordered polymeric structures [12], [13], [14].

Among the diverse biomass resources, oil palm kernel shell (OPKS) is a promising biomass precursor, particularly in Malaysia, where oil palm cultivation produces large volumes of OPKS waste. In fact, in 2022 alone, Malaysia has recorded 18.45 million tonnes of crude palm oil, a 1.9% increase compared to 18.12 million tonnes in 2021, which further contributes to OPKS accumulation [15]. On a global scale, there has been a significant increase in yearly palm oil production from 2013 to 2026, with Indonesia and Malaysia producing 46.7 and 20.2 million tonnes, respectively [16], [17]. The production of palm oil is proportionate to the production of OPKS. Hence, it is pertinent to convert OPKS into graphite and subsequently into rGO, as it not only provides a sustainable pathway for waste utilization but also supports the development of renewable carbon nanomaterials [18].

However, biomass-derived carbon contains impurities such as lignin, cellulose, hemicellulose, and inorganic residues, which can compromise the quality of the resulting graphite and rGO. Therefore, the use of suitable catalysts is essential to enhance graphitization efficiency and improve the crystallinity and properties of rGO.

## 2. METHODOLOGY

### 2.1 Preparation of Catalyst-Impregnated OPKS

Oil palm kernel shell (OPKS) biomass was collected from FELCRA palm oil plantation in Pauh, Perlis. It was thoroughly washed to remove dirt and residual oil, oven-dried, and crushed into small fragments. The dried OPKS was impregnated with aqueous iron(III) nitrate ($Fe(NO_3)_3$) solutions at different concentrations (10, 20, and 30 wt.%), while a non-impregnated sample served as a control. The impregnated biomass was dried overnight before further processing. The sample identification codes are summarized in Table 1.

**Table 1** Sample ID of graphite precursors prepared with various $Fe(NO_3)_3$ concentrations

| Catalyst concentration (wt.%) | Sample ID |
|---|---|
| 0 | $G_0$ (Control) |
| 10 | $G_{10}$ |
| 20 | $G_{20}$ |
| 30 | $G_{30}$ |

### 2.2 Synthesis of Graphite

Catalyst-impregnated OPKS samples were pyrolyzed in a tubular furnace under flowing nitrogen. The temperature was increased at a rate of 5 °C $min^{-1}$ to 800 °C and held for 3 h to promote catalytic graphitization. After cooling, the obtained char was treated with dilute hydrochloric acid to remove residual catalyst, repeatedly washed with distilled water until neutral pH, and oven-dried. Graphite yield was calculated gravimetrically.

### 2.3 Synthesis of Reduced Graphene Oxide (rGO)

Selected graphite samples, namely the catalyst-free control graphite ($G_0$) and the 20 wt.% $Fe(NO_3)_3$-derived graphite ($G_{20}$), were oxidized using a modified Hummers' method. Briefly, 3 g of graphite was pre-oxidized in concentrated $H_2SO_4$ containing $K_2S_2O_8$ and $P_4O_{10}$ at 80 °C for 4.5 h under continuous stirring. After cooling, the mixture was diluted with deionized water, filtered, and dried.

The pre-oxidized graphite was then further oxidized by slowly adding $KMnO_4$ into concentrated $H_2SO_4$ under ice-bath conditions (<5 °C) with continuous stirring for 2 h. Subsequently, deionized water and $H_2O_2$ were added to terminate the reaction. The resulting graphene oxide (GO) was filtered, washed with diluted HCl solution and deionized water until near-neutral pH, and dried at 80 °C.

For reduction, 1 g of GO was dispersed in 100 mL of deionized water and sonicated for 30 min. A 0.1 M $NaBH_4$ solution was then added, followed by stirring at 80 °C for 15 min. The obtained rGO was filtered, washed with deionized water, and dried at 80 °C for 3 h. The same procedure was applied to both $G_0$ and $G_{20}$ samples to obtain $rGO_0$ and $rGO_{20}$, respectively.

### 2.4 Characterization

The structural and morphological properties of the samples were characterized using X-ray diffraction (XRD, Bruker D2 Advance) to assess graphitic crystallinity and interlayer spacing, Raman spectroscopy (Thermo Fisher DXR3) to determine defect density ($I_D/I_G$ ratio) and graphitic order, and scanning electron microscopy (SEM, JEOL JSM-6010LV) to observe surface morphology and pore structure. Figure 1 shows the flow chart.

## 3. RESULT & DISCUSSION

### 3.1. Impact of Catalyst Concentration on Graphite Yield

The graphite yield was determined by measuring the weight of OPKS before and after the pyrolysis process. This measurement indicates both the extent of graphitization achieved and the degree of mass loss during thermal conversion. The findings are presented in Table 2.

**Table 2** Graphite yield from OPKS treated with different concentrations of $Fe(NO_3)_3$

| Sample ID | $Fe(NO_3)_3$ concentration (%) | Yield (%) |
|---|---|---|
| $G_0$ | 0 | 24.00 |
| $G_{10}$ | 10 | 31.23 |
| $G_{20}$ | 20 | 31.70 |
| $G_{30}$ | 30 | 32.34 |

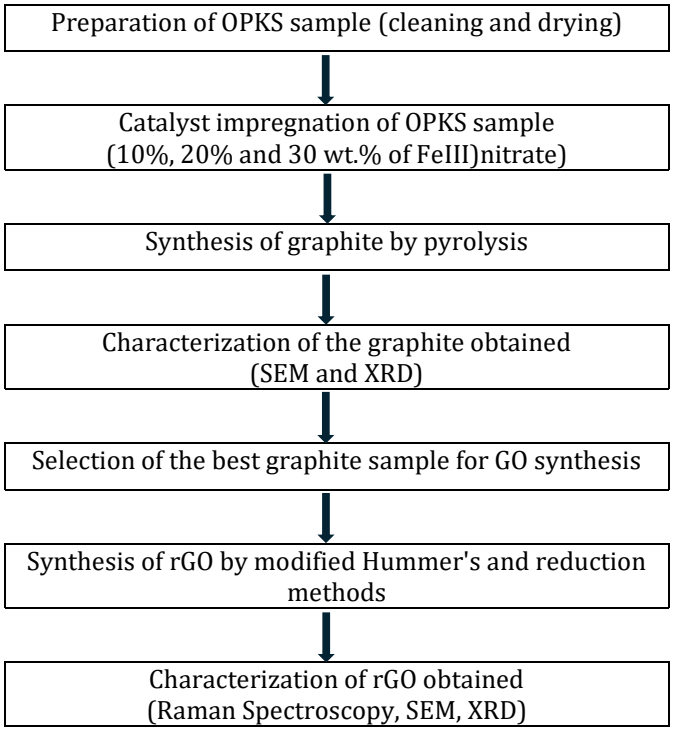


**Figure 1.** Flow chart of overall methodology.

The control sample ($G_0$), prepared without a catalyst exhibited the lowest yield (24%) while the $Fe(NO_3)_3$-impregnated samples: $G_{10}$, $G_{20}$, and $G_{30}$, achieved higher yields of 31.23%, 31.70%, and 32.34%, respectively. This increase demonstrates the catalytic role of $Fe(NO_3)_3$ in enhancing graphitization by promoting the thermal decomposition of OPKS and accelerating carbon structure reorganization, leading to improved carbon retention [19]. Without the catalyst, graphitisation is less efficient, resulting in greater volatilszation of carbonaceous species and a lower yield. However, the small yield differences among the catalyzed samples suggest that beyond a certain concentration of $Fe(NO_3)_3$, the catalytic effect reaches saturation, with limited improvements in carbon conversion efficiency [20].

The overall weight loss of OPKS during pyrolysis is mainly due to the evolution of gaseous by-products and the presence of residual ash. Thermal degradation of cellulose, hemicellulose, and lignin releases volatile species such as $CO_2$, CO, $CH_4$, and other hydrocarbons [21]. The $Fe(NO_3)_3$ catalyst promotes the formation of iron carbide ($Fe_3C$), which suppresses carbon volatilization by facilitating the conversion of carbon intermediates into stable graphite structures [22]. Additionally, impurities and moisture are eliminated during pyrolysis, while inorganic mineral residues remain as ash, further contributing to total mass loss.

According to Xia et. al. [23], iron carbide ($Fe_3C$) forms through the interaction between $Fe(NO_3)_3$ and the carbon-rich OPKS matrix at elevated temperatures. As $Fe(NO_3)_3$ decomposes, reduced iron species react with carbon atoms to produce $Fe_3C$, which acts as an active catalytic phase for graphitization by lowering the activation energy required for the rearrangement of amorphous carbon into ordered graphite layers. The catalytic mechanism not only promotes the rearrangement of carbon atoms but also helps preserve yield by preventing excessive carbon loss as gas. The end result is graphite with a higher degree of structural order and improved yield and quality.

The results indicate that $Fe(NO_3)_3$-catalyzed graphitization of OPKS-derived carbon significantly enhances graphite yield, which, on a related spectrum, has broader implications for applications in microfluidics, a technology sought out by many industries due to its ability to optimize fluid dynamics within microchannels and enhance analyte interactions (small things translate to cost-effectiveness) [24], [25]. The resultant rGO through optimized graphite yield, act as an advanced conductive substrate, enhancing

the performance of electrochemical sensors in microfluidic devices [26].

### 3.2. Effect of Catalyst Concentration on the Crystalline Structure of Graphite

Figure 2 displays the X-ray diffraction (XRD) patterns of graphite materials obtained at different $Fe(NO_3)_3$ catalyst concentrations. The diffraction profiles were compared to the standard graphite pattern from the International Centre for Diffraction Data (ICDD), showing characteristic reflections at approximately 2θ ≈ 26.5° (002), 42.2° (100), and 54.5° (004). Distinct peaks at around 26.5° and 42.2° were observed, while the (004) reflection was absent in all samples [27], indicating a high degree of structural disorder, stacking faults, or possible instrumental limitations [28].

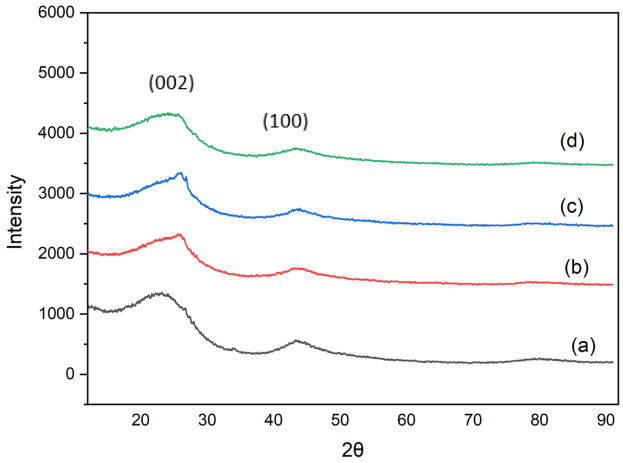


**Figure 2.** The XRD diffraction patterns of (a) $G_0$, (b) $G_{10}$, (c) $G_{20}$, and (d) $G_{30}$ graphite samples.

The sharpness and width of the (002) peak, which reflect interlayer spacing and stacking order, indicate the crystallinity levels of the samples. The order of sharpness was: $G_{30}$ < $G_0$ < $G_{10}$ < $G_{20}$, with $G_{20}$ exhibiting the most ordered structure. The (100) peak also showed minimal variation, suggesting that $Fe(NO_3)_3$ mainly influences interlayer stacking rather than in-plane crystal development [29].

$Fe(NO_3)_3$ enhances crystallinity by reducing defects and aligning carbon layers, resulting in sharper G20peaks$_0$. However, at higher concentration ($G_{30}$), the broader and less intense (002) peak suggests reduced structural order due to catalyst oversaturation, which may promote iron oxide agglomeration [30], and decrease catalytic efficiency. Excess catalyst can introduce impurities and disrupt carbon layer formation, diminishing graphitic order [31].

Table 3 details interlayer spacing and graphitization degrees, with values of 0.352 nm ($G_0$), 0.346 nm ($G_{10}$), 0.344 nm ($G_{20}$), and 0.350 nm ($G_{30}$). The smallest interlayer distance in $G_{20}$ matches the theoretical value for pristine graphite, confirming the highest degree of graphitization [32], while $G_0$ shows the widest spacing, reflecting a more disordered structure. The results prove the effectiveness of $Fe(NO_3)_3$ in promoting the structural reorganization of amorphous carbon into ordered graphitic domains, attributed to the in situ formation of iron carbide ($Fe_3C$) during pyrolysis [33], which in turns facilitates carbon layer alignment, reduces interlayer spacing, and enhances overall structural ordering.

**Table 3** The interlayer spacing ($d_{002}$) and degree of graphitization of graphite ($G_p$) of all graphite samples

| Sample ID | 2θ | θ | $d_{002}$ (nm) | $G_p$ (%) |
|---|---|---|---|---|
| $G_0$ | 25.28 | 12.64 | 0.352 | 30 |
| $G_{10}$ | 25.71 | 12.86 | 0.346 | 82 |
| $G_{20}$ | 25.85 | 12.93 | 0.344 | 97 |
| $G_{30}$ | 25.46 | 12.73 | 0.350 | 52 |

### 3.3. Influence of Catalyst Concentration on Graphite Morphology

XRD analysis indicated that $G_{20}$ represents the optimal catalyst concentration, showcasing the highest degree of graphitization and a well-ordered crystalline structure. The interlayer spacing in $G_{20}$ approaches that of pristine graphite, reflecting effective catalytic graphitization. Morphological characterization via SEM revealed there are differences in $G_{20}$ and the uncatalyzed sample, $G_0$, in surface irregularities, pore distribution, and folding. As shown in Figure 3, $G_{20}$ exhibits a more irregular surface with larger pores, a result of $Fe(NO_3)_3$'s catalytic action, which lowers activation energy for transforming disordered carbon precursors and enhances atomic mobility [34]. This activity

promotes the formation of larger voids and pores as carbon transitions from amorphous to graphitic forms [35].

In Figure 3, $G_{20}$'s surface features a more disordered topography with distorted shapes and expanded pore structures, consistent with findings by Othman et al. [36], who demonstrated that metal catalysts accelerate the structural reorganization of amorphous carbon, leading to improved graphitic ordering. Overall, the SEM results align with the XRD findings, confirming that $Fe(NO_3)_3$ significantly enhances the graphitization process of OPKS-derived carbon, resulting in superior structural and morphological characteristics.

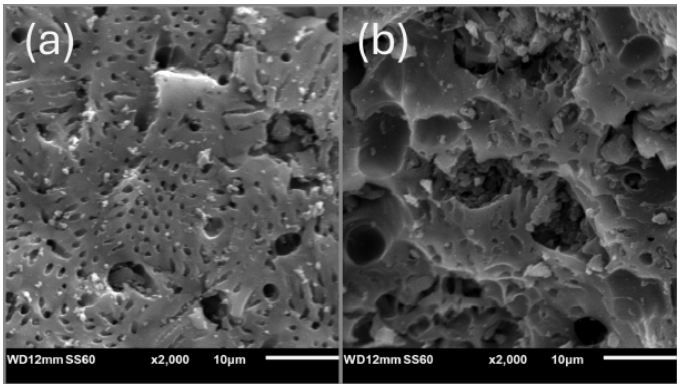


**Figure 3.** SEM images of (a) uncatalyzed graphite sample, $G_0$, and (b) graphite sample catalyzed with 20% $Fe(NO_3)_3$, $G_{20}$, at 2000x magnification.

### 3.4. Comparative Evaluation of rGO Quality Derived from Catalyzed and Uncatalyzed Graphite

Graphite sample, $G_{20}$, with its superior crystalline structure and highest degree of graphitization, was selected for synthesis into rGO. For comparison, graphite $G_0$ was transformed into rGO to assess the catalytic influence of $Fe(NO_3)_3$ during graphitization. Characterization analyses such as XRD – for graphitic crystallinity and interlayer spacing assessment, Raman spectroscopy – for defect density ($I_D/I_G$ ratio) and graphitic order determination, and SEM – for surface morphology, showed the structural properties of the samples. Figure 4 presents the XRD patterns of $rGO_0$ and $rGO_{20}$.

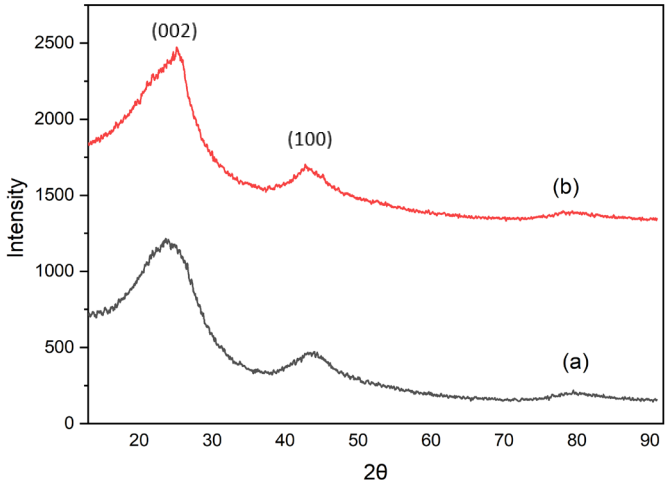


**Figure 4.** The XRD diffraction patterns of (a) $rGO_0$, and (b) $rGO_{20}$.

Both rGO samples exhibited significant peaks near 2θ = 25° (002) and 43° (100), confirming successful reduction of graphite oxide (ICDD Card 41-1487) [37]. Specifically, $rGO_{20}$ exhibited peaks at 24.05° and 42.74°, while $rGO_0$ showed peaks at 24.66° and 44.01°. The sharper peaks in $rGO_{20}$ indicate greater crystallinity and structural ordering, suggesting more effective removal of oxygen-containing functional groups compared to $rGO_0$. The superior quality of $rGO_{20}$ is attributed to the catalytic role of $Fe(NO_3)_3$, which facilitates a more ordered graphitic structure during $G_{20}$'s graphitization. The better-ordered precursor likely ensured uniform oxidation and reduction, minimizing over- or under-oxidized regions. As a result, $rGO_{20}$ showed enhanced crystallinity, stability, and fewer structural defects.

Table 4 summarizes XRD parameters, with $rGO_0$ showing a peak at 24.66° and interlayer spacing (d-spacing) of 0.363 nm, while $rGO_{20}$ showed a peak at 24.05° and a d-spacing of 0.368 nm. Though both values are higher than those of pristine graphene, they reflect residual oxygen functionalities or structural imperfections due to insufficient reduction [38], [39].

**Table 4** The interlayer spacing of the highest XRD peak

| Sample ID | 2θ | θ | $d_{002}$ (nm) |
|---|---|---|---|
| $rGO_0$ | 24.66 | 12.33 | 0.363 |
| $rGO_{20}$ | 24.05 | 12.03 | 0.368 |

Raman spectroscopy further assessed the structural order and defect density in the rGO samples. The spectra of both samples displayed the D band (~1350 $cm^{-1}$), associated with defects, and the G band (~1580 $cm^{-1}$), linked to $sp^2$-hybridized carbon [40]. For $rGO_0$, the D and G bands appeared at 1329.43 $cm^{-1}$ and 1570.85 $cm^{-1}$, respectively, while $rGO_{20}$ showed peaks at 1327.90 $cm^{-1}$ and 1569.32 $cm^{-1}$. The slight downshift of both bands in $rGO_{20}$ implies reduced strain and better graphitic ordering [41], [42], [43]. Notably, neither sample displayed a prominent 2D band around ~2700 $cm^{-1}$, indicating limited long-range graphitic ordering and a predominance of multilayer, defective graphene [44], [45]. This aligns with reports of biomass-derived reduced graphene oxide containing residual defects and incomplete $sp^2$ lattice restoration.

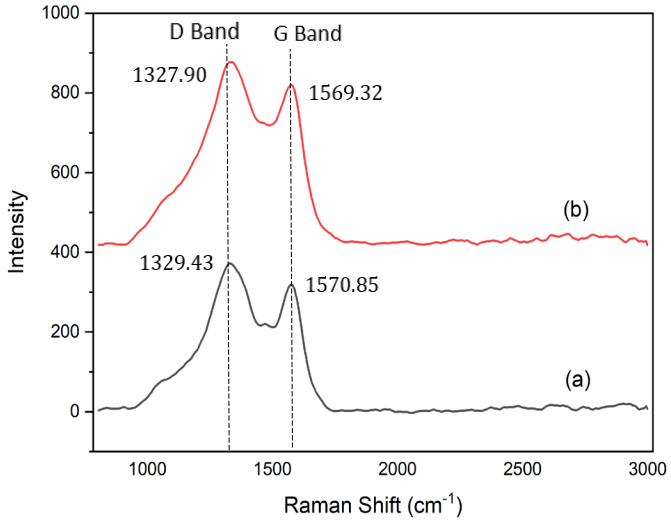


**Figure 5.** Raman spectra of (a) $rGO_0$, and (b) $rGO_{20}$.

Quantitative analysis in Table 5 indicates that both the D- and G-band intensities increased in $rGO_{20}$, while the intensity ratio ($I_D/I_G$) decreased from 1.155 ($rGO_0$) to 1.128 ($rGO_{20}$), reflecting lower defect density and enhanced graphitic character in the catalytically derived rGO [43].

**Table 5** Raman shift, peak Intensity, and $I_D/I_G$ ratio of rGO samples

| Sample ID | D-band | | G-Band | | $I_D/I_G$ Ratio |
|---|---|---|---|---|---|
| | Raman Shift ($cm^{-1}$) | Peak Intensity | Raman Shift ($cm^{-1}$) | Peak Intensity | |
| $rGO_0$ | 1329.43 | 378.08 | 1570.85 | 327.43 | 1.155 |
| $rGO_{20}$ | 1327.90 | 468.02 | 1569.32 | 415.69 | 1.128 |

SEM images in Figure 6 show clear differences in surface morphology. The $G_0$ sample presents a compact surface with small pores, indicating a less ordered structure, while $G_{20}$ features larger, well-defined pores [46]. After reduction, $rGO_0$ retains an irregular morphology, whereas $rGO_{20}$ exhibits a pronounced interconnected porous network with visible graphene layers, suggesting enhanced exfoliation [47]. The larger and more uniform pores in $G_{20}$ and $rGO_{20}$ correlate with higher graphitic order and crystallinity, aligning with XRD and Raman analyses. This morphology indicates a more effective reduction process, promoting the removal of oxygen functionalities and enhancing graphene layer exfoliation. In contrast, the smaller pores in $G_0$ and $rGO_0$ reflect lower graphitization levels and restricted reduction [48].

The quality of the precursor graphite is crucial, we can see this through the amorphous texture and small pores of uncatalyzed graphite ($G_0$) that limited exfoliation, while $G_{20}$'s crystalline structure enabled effective oxygen removal, resulting in $rGO_{20}$'s larger pores, better morphology, and fewer defects [49], emphasizing the relationship between precursor crystalline order and rGO quality.

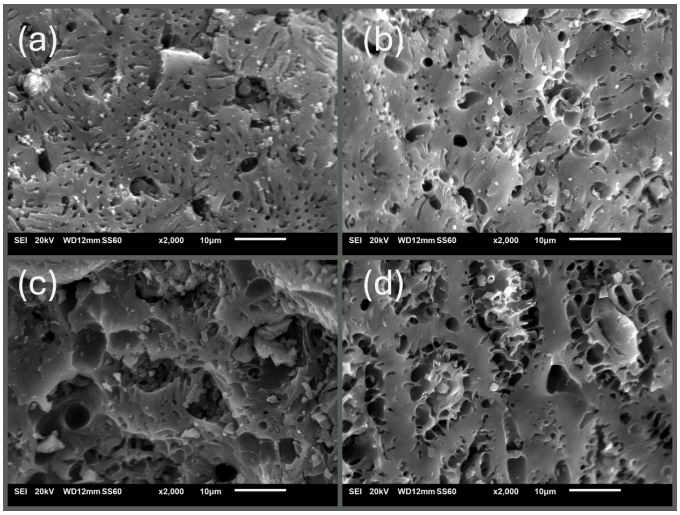


**Figure 6.** SEM images of graphite and its corresponding rGO product at 2000x magnification: (a)$G_0$, (b)$rGO_0$, (c)$G_{20}$, and (d) $rGO_{20}$.

## 4. CONCLUSION

This study highlights the effectiveness of $Fe(NO_3)_3$ as a catalyst for the graphitization of carbon derived from oil palm kernels, significantly enhancing both graphite yield and crystalline quality. The catalytic process involves lowering the activation energy required for carbon rearrangement and the temporary formation of iron carbide ($Fe_3C$), which serves as an active site, facilitating the development of well-ordered graphitic layers. Structural analyses using XRD, SEM, and Raman spectroscopy revealed that $G_{20}$, which was produced with 20 wt% $Fe(NO_3)_3$, along with its corresponding reduced graphene oxide ($rGO_{20}$), demonstrated superior crystallinity, improved lattice alignment, and reduced defect density when compared to the uncatalyzed samples. In short, the $Fe(NO_3)_3$-catalysed graphitisation process offers a promising, sustainable method for producing high-quality graphite and rGO from biomass precursors. These results underscore the significance of optimizing catalyst parameters to influence structural evolution and tailor the physicochemical characteristics of carbon materials. Future research should focus on linking catalytic parameters with electronic and electrochemical performance to establish relevant structure-property relationships in energy storage and advanced functional materials. The exceptional structural characteristics of $G_{20}$ and $rGO_{20}$ highlight their strong potential as electrode materials in energy storage devices, such as supercapacitors and batteries, paving way for sustainable, biomass-derived carbon materials to play a significant role in future energy technologies.

## ACKNOWLEDGMENTS

This research was supported by the Fundamental Research Grant Scheme (FRGS/1/2023/TK08/UNIMAP/02/8). The authors thank Universiti Malaysia Perlis for the facilities and support provided.

## REFERENCES

[1] R. Tarcan, O. Todor-Boer, I. Petrovai, C. Leordean, S. Astilean, and I. Botiz, "Reduced graphene oxide today," *pubs.rsc.orgR Tarcan, O Todor-Boer, I Petrovai, C Leordean, S Astilean, I BotizJournal of Materials Chemistry C, 2020•pubs.rsc.org*, vol. 8, no. 4, pp. 1198–1224, 2020, doi: 10.1039/C9TC04916A.

[2] D. Konios, M. M. Stylianakis, E. Stratakis, and E. Kymakis, "Dispersion behaviour of graphene oxide and reduced graphene oxide," *ElsevierD Konios, MM Stylianakis, E Stratakis, E KymakisJournal of colloid and interface science, 2014•Elsevier*, vol. 430, pp. 108–112, Sep. 2014, doi: 10.1016/J.JCIS.2014.05.033.

[3] N. Morimoto, T. Kubo, and Y. Nishina, "Tailoring the oxygen content of graphite and reduced graphene oxide for specific applications," *nature.comN Morimoto, T Kubo, Y NishinaScientific reports, 2016•nature.com*, vol. 6, Feb. 2016, doi: 10.1038/SREP21715.

[4] E. Muchuweni, E. T. Mombeshora, C. M. Muiva, and T. S. Sathiaraj, "Lithium-ion batteries: Recent progress in improving the cycling and rate performances of transition metal oxide anodes by incorporating graphene-based," *ElsevierE Muchuweni, ET Mombeshora, CM Muiva, TS SathiarajJournal of Energy Storage, 2023•Elsevier*, vol. 73, Dec. 2023, doi: 10.1016/J.EST.2023.109013.

[5] V. B. Mohan, R. Brown, K. Jayaraman, and D. Bhattacharyya, "Characterisation of reduced graphene oxide: Effects of reduction variables on electrical conductivity," *Elsevier*, vol. 193, no. C, pp. 49–60, Jul. 2015, doi: 10.1016/J.MSEB.2014.11.002.

[6] Abid, P. Sehrawat, S. S. Islam, P. Mishra, and S. Ahmad, "Reduced graphene oxide (rGO) based wideband optical sensor and the role of Temperature, Defect States and Quantum Efficiency," *nature.comAbid, P Sehrawat, SS Islam, P Mishra, S AhmadScientific reports, 2018•nature.com*, vol. 8, no. 1, Dec. 2018, doi: 10.1038/S41598-018-21686-2.

[7] Z. Li *et al.*, "Mechanisms of liquid-phase exfoliation for the production of graphene," *ACS PublicationsZ Li, RJ Young, C Backes, W Zhao, X Zhang, AA Zhukov, E Tillotson, AP Conlan, F DingACS nano, 2020•ACS Publications*, vol. 14, no. 9, pp. 10976–10985, Sep. 2020, doi: 10.1021/ACSNANO.0C03916.

[8] M. Ayhan, N. E.- Fullerenes, nanotubes and carbon, and undefined 2024, "Surface enhancement Raman spectroscopy of CVD graphene and graphene oxide," *Taylor & FrancisME Ayhan, N EmellerFullerenes, nanotubes and carbon nanostructures, 2024•Taylor & Francis*, vol. 32, no. 3, pp. 223–231, 2024, doi: 10.1080/1536383X.2023.2271586.

[9] Z. Benzait, P. Chen, and L. Trabzon, "Enhanced synthesis method of graphene oxide," *pubs.rsc.orgZ Benzait, P Chen, L TrabzonNanoscale Advances, 2021•pubs.rsc.org*, vol. 3, no. 1, pp. 223–230, Jan. 2021, doi: 10.1039/D0NA00706D.

[10] M. Abdollahifar, S. Doose, H. Cavers, and A. Kwade, "Graphite recycling from end-of-life lithium-ion batteries: processes and applications," *Wiley Online LibraryM Abdollahifar, S Doose, H Cavers, A KwadeAdvanced Materials Technologies, 2023•Wiley Online Library*, vol. 8, no. 2, Jan. 2023, doi: 10.1002/ADMT.202200368.

[11] M. D. Ibrahim, Y. A. Abakr, S. Gan, L. Y. Lee, and S. Thangalazhy-Gopakumar, "Intermediate Pyrolysis of Bambara Groundnut Shell (BGS) in Various Inert Gases (N2, CO2, and N2/CO2)," *mdpi.comMD Ibrahim, YA Abakr, S Gan, LY Lee, S Thangalazhy-GopakumarEnergies, 2022•mdpi.com*, vol. 15, no. 22, Nov. 2022, doi: 10.3390/EN15228421.

[12] Y. W. Yap *et al.*, "Recent advances in synthesis of graphite from agricultural bio-waste material: a review," *mdpi.comYW Yap, N Mahmed, MN Norizan, SZ Abd Rahim, MN Ahmad Salimi, K Abdul RazakMaterials, 2023•mdpi.com*, vol. 16, no. 9, May 2023, doi: 10.3390/MA16093601.

[13] M. Zhang, T. Xu, Q. Zhao, K. Liu, D. Liang, and C. Si, "Cellulose-based materials for carbon capture and conversion," *Elsevier*, vol. 10, Mar. 2024, doi: 10.1016/J.CCST.2023.100157.

[14] Z. Sun, R. Jiang, W. Hua, Q. Wei, Q. Yuan, and B. Yi, "Impact of Na at the low temperature Fe catalysis on high quality cellulose-based graphitic carbon," *ElsevierZ Sun, R Jiang, W Hua, Q Wei, Q Yuan, B YiJournal of Cleaner Production, 2024•Elsevier*, vol. 448, Apr. 2024, doi: 10.1016/J.JCLEPRO.2024.141740.

[15] C. B. S. Teh, S. S. Cheah, and H. Kulaveerasingam, "Development and validation of an oil palm model for a wide range of planting densities and soil textures in Malaysian growing conditions," *cell.comCBS Teh, SS Cheah, H KulaveerasingamHeliyon, 2024•cell.com*, vol. 10, no. 14, Jul. 2024, doi: 10.1016/J.HELIYON.2024.E32561.

[16] Foreign Agricultural Service, "Global Market Analysis: World Agricultural Production," Washington, DC, Apr. 2026. Accessed: May 04, 2026. [Online]. Available: https://apps.fas.usda.gov/psdonline/app/index.html#/app/downloads

[17] A. Ayoib, U. Hashim, and S. C. B. S. C. B. Gopinath, "Automated, high-throughput DNA extraction protocol for disposable label free, microfluidics integrating DNA biosensor for oil palm pathogen, Ganoderma boninense," *Process Biochemistry*, vol. 92, no. January, pp. 447–456, May 2020, doi: 10.1016/j.procbio.2020.02.003.

[18] J. P. Rajakal *et al.*, "Analysis of current state, gaps, and opportunities for technologies in the Malaysian oil palm estates and palm oil mills towards net-zero emissions," *cell.comJP Rajakal, FY Ng, A Zulkifli, BS How, J Sunarso, DKS Ng, V AndiappanHeliyon, 2024•cell.com*, vol. 10, no. 10, May 2024, doi: 10.1016/J.HELIYON.2024.E30768.

[19] Y. J. Choi, Y. S. Lee, J. H. Kim, and J. S. Im, "Optimization of Pore Characteristics of Graphite-Based Anode for Li-Ion Batteries by Control of the Particle Size Distribution," *mdpi.comYJ Choi, YS Lee, JH Kim, JS ImMaterials, 2023•mdpi.com*, vol. 16, no. 21, Nov. 2023, doi: 10.3390/MA16216896.

[20] S. Ike and R. Vander Wal, "Effect of carbonization methods on graphitization of soft and hard carbons," *ElsevierS Ike, R Vander WalCarbon Trends, 2024•Elsevier*, vol. 16, Sep. 2024, doi: 10.1016/J.CARTRE.2024.100382.

[21] X. Chen *et al.*, "Graphitization of graphene oxide films under pressure," *ElsevierX Chen, X Deng, NY Kim, Y Wang, Y Huang, L Peng, M Huang, X Zhang, X Chen, D LuoCarbon, 2018•Elsevier*, vol. 132, pp. 294–303, Jun. 2018, doi: 10.1016/J.CARBON.2018.02.049.

[22] S. I. Talabi, A. P. Luz, V. C. Pandolfelli, and A. A. Lucas, "Structural evolution during the catalytic graphitization of a thermosetting refractory binder and oxidation resistance of the derived carbons," *ElsevierSI Talabi, AP Luz, VC Pandolfelli, AA LucasMaterials Chemistry and Physics, 2018•Elsevier*, vol. 212, pp. 113–121, Jun. 2018, doi: 10.1016/J.MATCHEMPHYS.2018.03.029.

[23] S. Xia *et al.*, "Fe–Co based synergistic catalytic graphitization of biomass: Influence of the catalyst type and the pyrolytic temperature," *ElsevierS Xia, H Yang, W Lu, N Cai, H Xiao, X Chen, Y Chen, X Wang, S Wang, P Wu, H ChenEnergy, 2022•Elsevier*, vol. 239, Jan. 2022, doi: 10.1016/J.ENERGY.2021.122262.

[24] A. Ayoib, U. Hashim, S. C. B. Gopinath, V. Thivina, and M. K. M. Arshad, "Design and fabrication of PDMS microfluidics device for rapid and label-free DNA detection," *Applied Physics A*, vol. 126, no. 3, p. 193, Mar. 2020, doi: 10.1007/s00339-020-3337-7.

[25] A. Ayoib *et al.*, "Cost-Effective Fabrication of Polydimethylsiloxane (PDMS) Microfluidics for Point-of-Care Application," *International Journal of Nanoelectronics and Materials (IJNeaM)*, vol. 17, no. June, pp. 143–151, Jun. 2024, doi: 10.58915/ijneam.v17iJune.848.

[26] A. Ayoib, S. A. Shamsuddin, N. A. Parmin, and D. A. A. R. Rajapaksha, "Comparative Evaluation of CTAB and AP1 Buffers in On-Chip DNA Extraction of Pathogenic Fungus for Microfluidic Interdigitated-Electrode Biosensing," *International Journal of Nanoelectronics and Materials (IJNeaM)*, vol. 18, no. December, pp.

279–288, Dec. 2025, doi: 10.58915/ijneam.v18iDecember.2840.

[27] L. Gai, J. Li, Q. Wang, R. Tian, and K. Li, "Evolution of biomass to porous graphite carbon by catalytic graphitization," *ElsevierL Gai, J Li, Q Wang, R Tian, K LiJournal of Environmental Chemical Engineering, 2021•Elsevier*, vol. 9, no. 6, Dec. 2021, doi: 10.1016/J.JECE.2021.106678.

[28] B. P. Thapaliya, H. Luo, P. Halstenberg, H. M. Meyer, J. R. Dunlap, and S. Dai, "Low-cost transformation of biomass-derived carbon to high-performing nano-graphite via low-temperature electrochemical graphitization," *ACS PublicationsBP Thapaliya, H Luo, P Halstenberg, HM Meyer III, JR Dunlap, S DaiACS Applied Materials & Interfaces, 2021•ACS Publications*, vol. 13, no. 3, pp. 4393–4401, Jan. 2021, doi: 10.1021/ACSAMI.0C19395.

[29] E. Thompson, A. E. Danks, L. Bourgeois, and Z. Schnepp, "Iron-catalyzed graphitization of biomass," *pubs.rsc.orgE Thompson, AE Danks, L Bourgeois, Z SchneppGreen Chemistry, 2015•pubs.rsc.org*, vol. 17, no. 1, pp. 551–556, Jan. 2015, doi: 10.1039/C4GC01673D.

[30] S. Xia *et al.*, "Synthesis and formation mechanism of biomass-based mesoporous graphitic carbon," *ElsevierS Xia, N Cai, J Wu, H Xiao, J Hu, X Chen, Y Chen, H Yang, X Wang, H ChenFuel Processing Technology, 2020•Elsevier*, vol. 209, Dec. 2020, doi: 10.1016/J.FUPROC.2020.106543.

[31] P. Liu, W. Du, X. Liu, L. Zhang, and Z. Chen, "Sustainable catalytic graphitization of biomass to graphitic porous carbon by constructing permeation network with organic ligands," *Elsevier*, vol. 64, pp. 259–270, Dec. 2023, doi: 10.1016/J.CJCHE.2023.06.025.

[32] Y. Saito, T. Yoshikawa, S. Bandow, M. Tomita, and T. Hayashi, "Interlayer spacings in carbon nanotubes," *APSY Saito, T Yoshikawa, S Bandow, M Tomita, T HayashiPhysical Review B, 1993•APS*, vol. 48, no. 3, pp. 1907–1909, 1993, doi: 10.1103/PHYSREVB.48.1907.

[33] N. A. Banek, K. R. McKenzie, D. T. Abele, and M. J. Wagner, "Sustainable conversion of biomass to rationally designed lithium-ion battery graphite," *nature.comNA Banek, KR McKenzie Jr, DT Abele, MJ WagnerScientific Reports, 2022•nature.com*, vol. 12, no. 1, Dec. 2022, doi: 10.1038/S41598-022-11853-X.

[34] M. Mundszinger, S. Farsi, M. Rapp, U. Golla-Schindler, U. Kaiser, and M. Wachtler, "Morphology and texture of spheroidized natural and synthetic graphites," *ElsevierM Mundszinger, S Farsi, M Rapp, U Golla-Schindler, U Kaiser, M WachtlerCarbon, 2017•Elsevier*, vol. 111, pp. 764–773, Jan. 2017, doi: 10.1016/J.CARBON.2016.10.060.

[35] J. X. Gao, B. Q. Wei, D. D. Li, and K. He, "Nucleation and growth characteristics of graphite spheroids in bainite during graphitization annealing of a medium carbon steel," *ElsevierJX Gao, BQ Wei, DD Li, K HeMaterials characterization, 2016•Elsevier*, vol. 118, pp. 1–8, Aug. 2016, doi: 10.1016/J.MATCHAR.2016.05.003.

[36] R. Othman, A. S. Kamal, and N. H. Jabarullah, "The effect of changing graphitization temperature toward bio-graphite from palm kernel shell," *sciendo.comR Othman, AS Kamal, NH JabarullahProduction Engineering Archives, 2021•sciendo.com*, vol. 27, no. 2, pp. 124–129, Jun. 2021, doi: 10.30657/PEA.2021.27.16.

[37] R. Al-Gaashani, A. Najjar, Y. Zakaria, S. Mansour, and M. A. Atieh, "XPS and structural studies of high quality graphene oxide and reduced graphene oxide prepared by different chemical oxidation methods," *ElsevierR Al-Gaashani, A Najjar, Y Zakaria, S Mansour, MA AtiehCeramics International, 2019•Elsevier*, vol. 45, no. 11, pp. 14439–14448, Aug. 2019, doi: 10.1016/J.CERAMINT.2019.04.165.

[38] R. Futamura *et al.*, "Staggered structural dynamic-mediated selective adsorption of H2O/D2O on flexible graphene oxide nanosheets," *nature.comR Futamura, T Iiyama, T Ueda, PA Bonnaud, FX Coudert, A Furuse, H Tanaka, RJM PellenqNature Communications, 2024•nature.com*, vol. 15, no. 1, Dec. 2024, doi: 10.1038/S41467-024-47838-9.

[39] M. Q. Zhao *et al.*, "Unstacked double-layer templated graphene for high-rate lithium–sulphur batteries," *nature.comMQ Zhao, Q Zhang, JQ Huang, GL Tian, JQ Nie, HJ Peng, F WeiNature communications, 2014•nature.com*, vol. 5, Mar. 2014, doi: 10.1038/NCOMMS4410.

[40] C. Neumann *et al.*, "Raman spectroscopy as probe of nanometre-scale strain variations in graphene," *nature.comC Neumann, S Reichardt, P Venezuela, M Drögeler, L Banszerus, M Schmitz, K WatanabeNature communications, 2015•nature.com*, vol. 6, Sep. 2015, doi: 10.1038/NCOMMS9429.

[41] J. Bin Wu *et al.*, "Resonant Raman spectroscopy of twisted multilayer graphene," *nature.comJB Wu, X Zhang, M Ijäs, WP Han, XF Qiao, XL Li, DS Jiang, AC Ferrari, PH TanNature communications, 2014•nature.com*, vol. 5, 2014, doi: 10.1038/NCOMMS6309.

[42] T. Lee, F. A. Mas'Ud, M. J. Kim, and H. Rho, "Spatially resolved Raman spectroscopy of defects, strains, and strain fluctuations in domain structures of monolayer graphene," *nature.comT Lee, FA Mas' ud, MJ Kim, H RhoScientific reports, 2017•nature.com*, vol. 7, no. 1, Dec. 2017, doi: 10.1038/S41598-017-16969-Z.

[43] S. S. Nanda, D. K. Yi, and K. Kim, "Study of antibacterial mechanism of graphene oxide using Raman spectroscopy," *nature.comSS Nanda, DK Yi, K KimScientific reports, 2016•nature.com*, vol. 6, Jun. 2016, doi: 10.1038/SREP28443.

[44] S. Watcharamaisakul, N. Janphuang, W. C.-Nanomaterials, and undefined 2025, "Synthesis of Turbostratic Graphene Derived from Biomass Waste Using Long Pulse Joule Heating Technique," *mdpi.comS Watcharamaisakul, N Janphuang, W Chueangam, K Srisom, A RueangwittayanonNanomaterials, 2025•mdpi.com*, Accessed: Apr. 28, 2026. [Online]. Available: https://www.mdpi.com/2079-4991/15/6/468.

[45] R. A. Mensah *et al.*, "The facile conversion of waste biomass into few-layer graphene oxide," *nature.comRA Mensah, V Shanmugam, E Kaynak, D Sokol, J Wahl, KC Le, Y Zhang, L JiangScientific Reports, 2025•nature.com*, vol. 15, no. 1, Dec. 2025, doi: 10.1038/S41598-025-93037-X.

[46] A. C. Ferrari and D. M. Basko, "Raman spectroscopy as a versatile tool for studying the properties of graphene," *nature.comAC Ferrari, DM BaskoNature nanotechnology, 2013•nature.com*, vol. 8, no. 4, pp. 235–246, 2013, doi: 10.1038/NNANO.2013.46.

[47] D. Lin *et al.*, "Layered reduced graphene oxide with nanoscale interlayer gaps as a stable host for lithium metal anodes," *nature.comD Lin, Y Liu, Z Liang, HW Lee, J Sun, H Wang, K Yan, J Xie, Y CuiNature nanotechnology, 2016•nature.com*, vol. 11, no. 7, pp. 626–632, Jul. 2016, doi: 10.1038/NNANO.2016.32.

[48] Y. Chen *et al.*, "Ultra-fast self-assembly and stabilization of reactive nanoparticles in reduced graphene oxide films," *nature.comY Chen, GC Egan, J Wan, S Zhu, RJ Jacob, W Zhou, J Dai, Y Wang, VA Danner, Y Yao, K FuNature communications, 2016•nature.com*, vol. 7, Aug. 2016, doi: 10.1038/NCOMMS12332.

[49] J. Sen Li *et al.*, "Coupled molybdenum carbide and reduced graphene oxide electrocatalysts for efficient hydrogen evolution," *nature.comJS Li, Y Wang, CH Liu, SL Li, YG Wang, LZ Dong, ZH Dai, YF Li, YQ LanNature communications, 2016•nature.com*, vol. 7, Apr. 2016, doi: 10.1038/NCOMMS11204.